Turkish Journal of Electrical Engineering & Computer Sciences

http://journals.tubitak.gov.tr/elektrik/

Research Article

Turk J Elec Eng & Comp Sci
(2017) 25: 2885 – 2896

doi:10.3906/elk-1604-40

Analysis of a joined split-ring FSS structure characterized by three resonant frequencies and a tuned enhanced band using the WCIP method

Manel AOUISSI[1,*], Mohammed TITAOUINE[1,2], Thayuan Rolim de SOUSA[3], Ibtissem ADOUI[2], Alfrêdo GOMES NETO[3], Henri BAUDRAND[4]

[1]Department of Electronics, Faculty of Technology, University of Batna, Batna, Algeria
[2]Department of Electronics, Faculty of Science and Technology, Bordj Bou-Arréridj University, El Anasseur, Algeria
[3]Federal Institute of Education, Science, and Technology of Paraíba (IFPB), João Pessoa, Paraíba, Brazil
[4]Department of Electronics, Faculty of Electronics, University of Toulouse, Toulouse, France

Received: 04.04.2016 • **Accepted/Published Online:** 11.11.2016 • **Final Version:** 30.07.2017

Abstract: This work presents the analysis of a joined split-ring frequency selective surface (FSS) for X-band applications using the wave concept iterative procedure (WCIP). When the incident normal plane wave is polarized in the x direction, the joined split-ring FSS shows three rejecting bands at 9 GHz, 10.5 GHz, and 11.5 GHz simultaneously with bandwidths of 3.11 GHz, 0.6 GHz, and 1.13 GHz, respectively. Moreover, one rejecting band at 6.5 GHz is present when the FSS is fed with a normal plane excited in the y direction. In addition, the different resonant frequencies can be tuned independently to give rise to a tuned enhanced band. An FSS with four rejecting bands is obtained when the metallic notch is placed on the lower coupling metallic strip. The joined split-ring FSS is manufactured and measured. The simulated results obtained using the WCIP are compared to the measured results and COMSOL Multiphysics results and good agreement is obtained.

Key words: Joined split-ring frequency selective surface, concept iterative procedure method, resonant frequency tuning, band enhancement

1. Introduction

There are many applications where frequency selective surfaces (FSSs) can be found, such as reflectors or filters [1–3]. The dual polarized behavior of planar structures is studied for the sake of flexibility in antennas [4] and FSSs [5]. In this paper a novel joined split-ring FSS is presented for dual polarized spatial communications. It can be used for triband applications if the FSS is fed with an x polarized plane wave and for mono-band applications when a y polarized source is used. The analysis of this structure is carried out using the wave concept iterative procedure (WCIP) detailed in [6,7]. The use of a split-ring resonator and notches in microstrip antennas and filters provides a large rejecting band [8,9]. Hence, joining the split-ring in the presented FSS can allow an enhanced adjustable rejecting band in addition to multiresonant frequencies. An additional rejecting band is generated by a simple position changing of the FSS metallic notch. A parametric study allows the determination of the FSS dimensions affecting the three resonant frequencies.

One joined split-ring FSS is manufactured and measured for both x and y polarizations. The WCIP results are compared to measurements and COMSOL-4.3b results and good agreement is recorded.

*Correspondence: aouissimnl@gmail.com

2. Theory: WCIP formulation

The WCIP method is a full wave method based on transverse wave formulation and on an iterative procedure repeated until convergence is reached. The waves' information is collected at interface Ω containing the electric circuit made up by a metallic domain etched on a dielectric medium and separating two dielectric media. The scattered waves at the interfaces are related to the incident waves by the use of a scattering operator $\hat{S_\Omega}$ defined in the spatial domain using the boundary conditions at the interface characterizing the metallic and the dielectric domains. Reflection operator $\hat{\Gamma_i}$, defined in the modal domain, intervenes to relate the diffracted waves to the incident waves of the next iteration. The iterative procedure is shown in Figure 1.

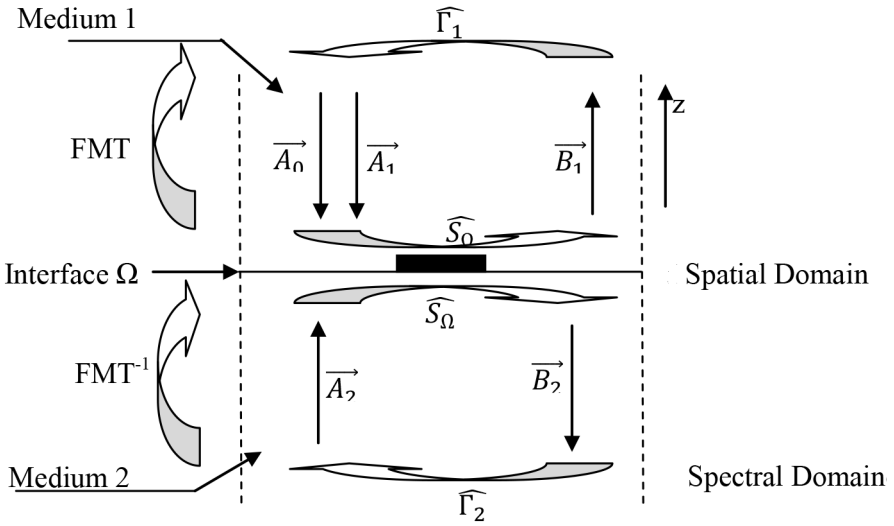

Figure 1. Iterative procedure.

The incident waves $\vec{A}_i$ and the scattered waves $\vec{B}_i$ are calculated from the tangential electric and magnetic fields $\vec{E}_{Ti}$ and $\vec{H}_{Ti}$ as [5–7]:

$$\vec{A}_i = \frac{1}{2\sqrt{Z_{0i}}}\left(\vec{E}_{Ti} + Z_{0i}\,\vec{J}_i\right), \tag{1}$$

$$\vec{B}_i = \frac{1}{2\sqrt{Z_{0i}}}\left(\vec{E}_{Ti} - Z_{0i}\vec{J}_i\right), \tag{2}$$

where i indicates medium 1 or 2 separated by interface Ω. Z_{0i} is the characteristic impedance of the same medium i. $\vec{J}_i$ is the surface current density obtained from the tangential magnetic field $\vec{H}_{Ti}$ by a simple rotation as a result of the vector product of the normal vector $\vec{n}$ and the magnetic field $\vec{H}_{Ti}$.

The tangential electric field and the surface current density can be calculated from [10]:

$$\vec{E}_{Ti} = \sqrt{Z_{0i}}\left(\vec{A}_i + \vec{B}_i\right), \tag{3}$$

$$\vec{J}_i = (1/\sqrt{Z_{0i}})\left(\vec{A}_i - \vec{B}_i\right). \tag{4}$$

Scattered waves $\vec{B}_i$ will be reflected from the closing impedances to generate incident waves $\vec{A}_i$ for the next

iteration after adding incident source waves $\vec{A}_0$. Incident waves $\vec{A}_i$ can be calculated by:

$$\begin{vmatrix} \vec{A}_1 \\ \vec{A}_2 \end{vmatrix} = \begin{bmatrix} \hat{\Gamma}_1 & 0 \\ 0 & \hat{\Gamma}_2 \end{bmatrix} \begin{vmatrix} \vec{B}_1 \\ \vec{B}_2 \end{vmatrix} + \begin{vmatrix} \vec{A}_0 \\ \vec{0} \end{vmatrix}, \tag{5}$$

where $\hat{\Gamma}_i$ is the reflection coefficient of the closing impedances of medium i.

2.1. Scattering operator $\hat{S_\Omega}$ determination

$\hat{S_\Omega}$ is a scattering operator defined in the spatial domain. The two domains characterizing interface Ω of the studied FSSs are the dielectric domain D and the metal domain H. Scattering operator $\hat{S_\Omega}$ is taken as a superposition of the metallic domain scattering operator $\hat{S_M}$ and the dielectric domain scattering operator $\hat{S_D}$. The scattering operator is determined using the geometry of the FSS at interface Ω and ensuring the satisfaction of the boundary conditions at the dielectric and metallic domains. The indicating dielectric domain function H_D and the indicating metallic domain function H_M can be represented using Heaviside unit steps as:

$$H_D = \begin{cases} 1 & \text{on the dielectric} \\ 0 & \text{otherwise} \end{cases}, \tag{6}$$

$$H_M = \begin{cases} 1 & \text{on the metal} \\ 0 & \text{otherwise} \end{cases}. \tag{7}$$

The boundary conditions on the metal are verified on the domain H_M if the transverse electric field is null at the two sides of interface Ω such as [11]:

$$\vec{E}_1 = \vec{E}_2 = \vec{0}. \tag{8}$$

Replacing Eq. (8) in Eq. (3), metal domain scattering operator $\hat{S_M}$ can be obtained as:

$$\left[\hat{S_M}\right] = \begin{vmatrix} -H_M & 0 \\ 0 & -H_M \end{vmatrix}. \tag{9}$$

In dielectric domain D, to satisfy the boundary conditions on H_D the current density should be null on the dielectric domain and the electric field should be the same at the two sides of interface Ω in such a way that [11]:

$$\begin{cases} \vec{J}_{tot} = \vec{J}_1 + \vec{J}_2 = \vec{0} \\ \vec{E}_1 = \vec{E}_2 \end{cases}, \tag{10}$$

where $\vec{J}_1$ and $\vec{J}_2$ are the current densities at the two sides of interface Ω. $\vec{E}_1$ and $\vec{E}_2$ are the tangential electric fields at the two sides of interface Ω.

Replacing Eq. (10) in Eqs. (3) and (4), the dielectric domain scattering operator $\hat{S_D}$ can be obtained in terms of the dielectric domain indicating function H_D as:

$$\left[\hat{S_D}\right] = \begin{vmatrix} \frac{1-N^2}{1+N^2} H_D & \frac{2N}{1+N^2} H_D \\ \frac{2N}{1+N^2} H_D & -\frac{1-N^2}{1+N^2} H_D \end{vmatrix}, \tag{11}$$

where N is a constant obtained when solving for the dielectric domain scattering operator $\hat{S_D}$ for the dielectric boundary conditions at interface Ω. N $=\sqrt{\frac{Z_{01}}{Z_{02}}}$, with Z_{01} and Z_{02} indicating the characteristic impedance of medium 1 and 2, respectively.

The total scattering operator $\hat{S_\Omega}$ is then given as:

$$\hat{S_\Omega} = \hat{S_M} + \hat{S_D}. \tag{12}$$

2.2. Reflection operator determination

$\hat{\Gamma}_i$ is the reflection operator of the ith medium; it is diagonal since the modes are independent from each other and it is characterized by a specific reflection coefficient depending on the mode type, TE or TM. The nondetermination of reflection coefficient Γ in the spatial domain leads to a need to use the reflection coefficient in the modal domain because of its definition in the modes basis. As a result, a transition from the spatial domain to the modal domain is predominant. To enable this operation, a transform known as the fast modal transform (FMT) is to be used. The inverse operation can take place using the FMT^{-1} to go back to the spatial domain.

The TE$_{mn}$ and TM$_{mn}$ mode reflection coefficients are given by [6,7]:

$$\begin{cases} \Gamma i_{mn}^{TE} = \frac{1-Z_{0i}Yi_{mn}^{TE}}{1+Z_{0i}Yi_{mn}^{TE}} \\ \Gamma i_{mn}^{TM} = \frac{1-Z_{0i}Yi_{mn}^{TM}}{1+Z_{0i}Yi_{mn}^{TM}} \end{cases}, \tag{13}$$

where Yi_{mn}^{TE} and Yi_{mn}^{TM} are respectively the admittance of the mnth TE and TM mode admittance at medium i. Z$_{0i}$ is the ith medium characteristic impedance. When no closing ends exist, Yi_{mn}^{TE} and Yi_{mn}^{TM} of medium $i$can be calculated by [11,12]:

$$\hat{Y}i_{mn}^{TM} = \frac{j\omega\varepsilon_0\varepsilon_{ri}}{\overset{(i)}{\gamma_{mn}}}, \tag{14}$$

$$\hat{Y}i_{mn}^{TE} = \frac{\overset{(i)}{\gamma_{mn}}}{j\omega\mu_0}. \tag{15}$$

$\overset{(i)}{\gamma_{mn}}$ is the propagation constant of medium i for the mnth TE and TM modes and it is given as:

$$\overset{(i)}{\gamma_{mn}} = \sqrt{\left(\frac{2\,\pi m}{a}\right)^2 + \left(\frac{2\pi n}{b}\right)^2 - k_0^2\,\varepsilon_{ri}}. \tag{16}$$

$\varepsilon_0\varepsilon_{ri}$, and μ_0 are the permittivity of the vacuum, the relative permittivity of medium i, and the permeability of the vacuum, respectively. a and b are the dimensions of the FSS unit cell along the x and y directions.

2.3. Fast modal transform

Going from the spatial domain to the modal domain and back to the spatial domain is achieved by the use of the fast modal transform pair FMT/FMT^{-1}.

The determination of the FMT/FMT^{-1} pair is detailed in [6]:

$$FMT\left(\left|\begin{array}{c} E_x(x,y) \\ E_y(x,y) \end{array}\right|\right) = \left|\begin{array}{c} B_{mn}^{TE} \\ B_{mn}^{TE} \end{array}\right| = \left|\begin{array}{cc} K_{ymn} & -K_{xmn} \\ K_{xmn} & K_{ymn} \end{array}\right| FFT2\left(\left|\begin{array}{c} E_x(x,y) \\ E_y(x,y) \end{array}\right|\right), \tag{17}$$

$$FMT^{-1}\left|\begin{array}{c} B_{mn}^{TE} \\ B_{mn}^{TE} \end{array}\right| = \left(\left|\begin{array}{c} E_x(x,y) \\ E_y(x,y) \end{array}\right|\right) = FFT2\left(\left|\begin{array}{cc} K_{ymn} & K_{xmn} \\ -K_{xmn} & K_{ymn} \end{array}\right| \left|\begin{array}{c} E_x(x,y) \\ E_y(x,y) \end{array}\right|\right), \tag{18}$$

where k_{mn}, k_{xmn}, and k_{ymn} are constants given by $\mathbf{k_{mn}}=\frac{\mathbf{1}}{\sqrt{\left(\frac{\mathbf{m}}{\mathbf{a}}\right)^{\mathbf{2}}+\left(\frac{\mathbf{n}}{\mathbf{b}}\right)^{\mathbf{2}}}}$, $\mathbf{k_{xmn}}=\frac{\mathbf{m}}{\mathbf{a}}\mathbf{k_{mn}}$, and $\mathbf{k_{ymn}}=\frac{\mathbf{n}}{\mathbf{b}}\mathbf{k_{mn}}$, respectively.

3. Geometry of the joined split-ring FSS and the measurement setup

The WCIP method is used to characterize the joined split-ring FSS structure manufactured as an array of 10 $\times$ 10 unit cells shown in Figure 2a. The interface of the FSS unit cell of Figure 2b is divided into 250 $\times$ 250 pixels. The iterative procedure is stopped after 300 iterations.

The used measurement setup is shown in Figure 2c. It consists of an AGILENT N5230A two-port network analyzer and two horn antennas of the type WR-137 with a nominal 20 dB gain used in the operating frequency band of 4.5–9.0 GHz even though the nominal band is 5.85–8.2 GHz. To cover the remaining used operating frequency band a second type of horn antennas of type WR-90 with a nominal gain of 15 dB is used in the operating frequency band of 7–14 GHz even though the nominal band is 8.2–12.4 GHz. The band of 7–9 GHz represents the common operating band and provides the most precise measured results.

4. Simulation and measurement results

Depicted in Figure 3 is the transmitted power versus the operating frequency for the joined split-ring FSS of Figure 1a obtained by the WCIP method, COMSOL Multiphysics 4.3.b, and measurements for both x and y polarizations. The dimensions of the FSS are given in Table 1. The three x polarized rejecting bands occur at about 9 GHz, 10.5 GHz, and 11.5 GHz and one band takes place at 6.5 GHz when the source is y polarized. Good agreement is observed between COMSOL simulations and measurements. For WCIP results the differences as compared to the measurements and COMSOL results are related to the number of used points to describe interface Ω and to the limited number of used iterations to stop the WCIP method's procedure.

Table 1. Parameters of the joined split-ring FSS.

L_1	L_2	L_3	L_4	L_5	L_6	L_7	L_8	h	ε_r	w
7.5 mm	12 mm	5 mm	3 mm	6 mm	5 mm	6 mm	7.5 mm	1 mm	4.4	2 mm

In Figure 4 the joined split-ring FSS is characterized by the WCIP method and COMSOL Multiphysics for different values of L_4 varying from 2.6 mm to 3 mm, maintaining the remaining FSS dimensions constant when the FSS structure is excited with an x polarized incident plane wave. Only the lowest resonant frequency is considerably affected, permitting a fine-tuning of the lowest rejecting band frequency position. The central and the highest resonant frequencies are slightly affected. As compared to the variations in the lowest resonant frequency, the effect of L_4 can be considered as a way for the FSS lowest resonant frequency to be significantly

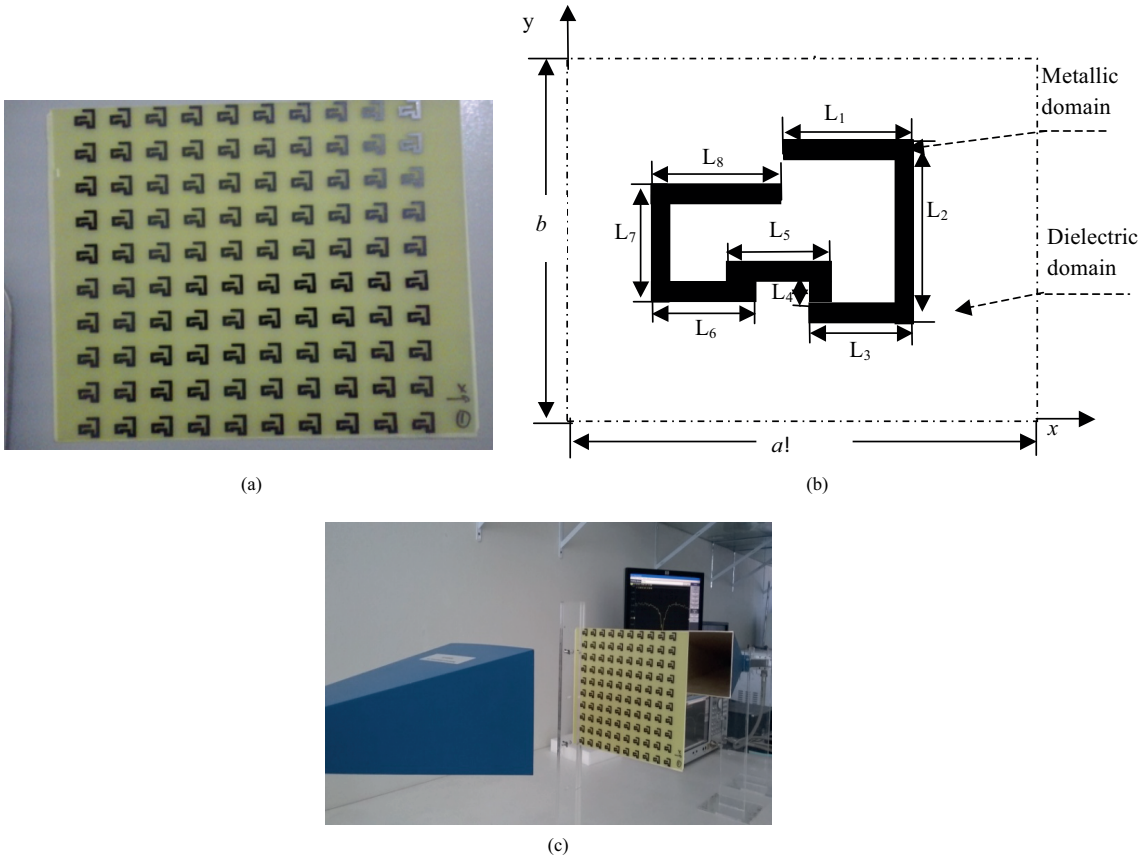

Figure 2. Joined split-ring FSS: (a) realized FSS with array of 10 × 10 unit cells, (b) geometry of unit cell and dimensions, (c) measurement setup.

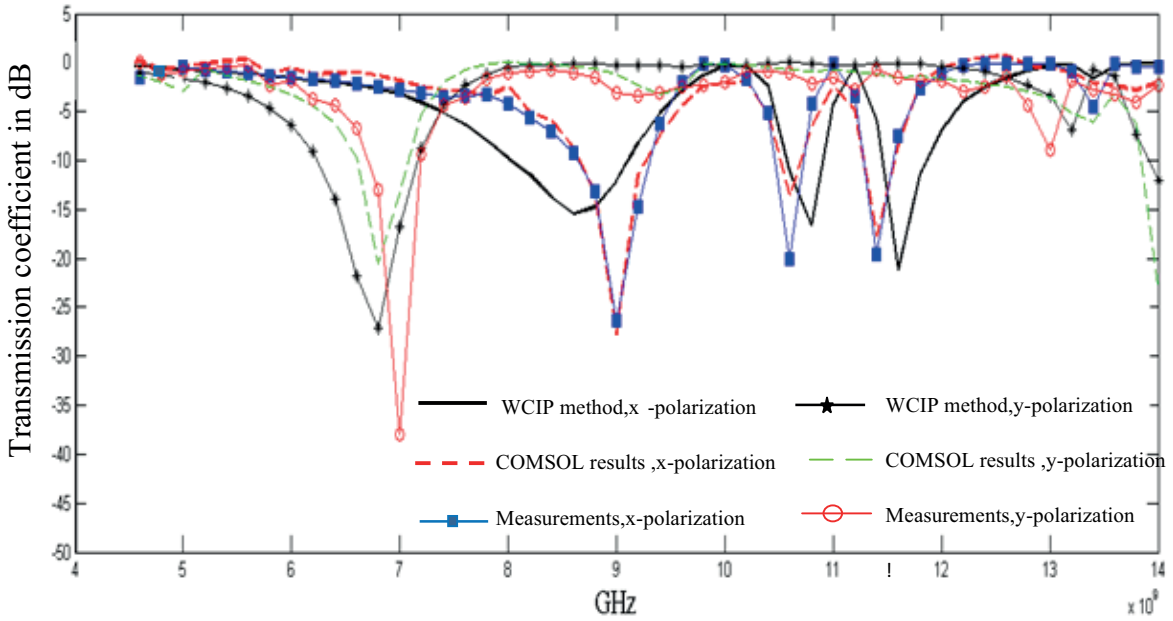

Figure 3. Variation of the transmitted power versus frequency.

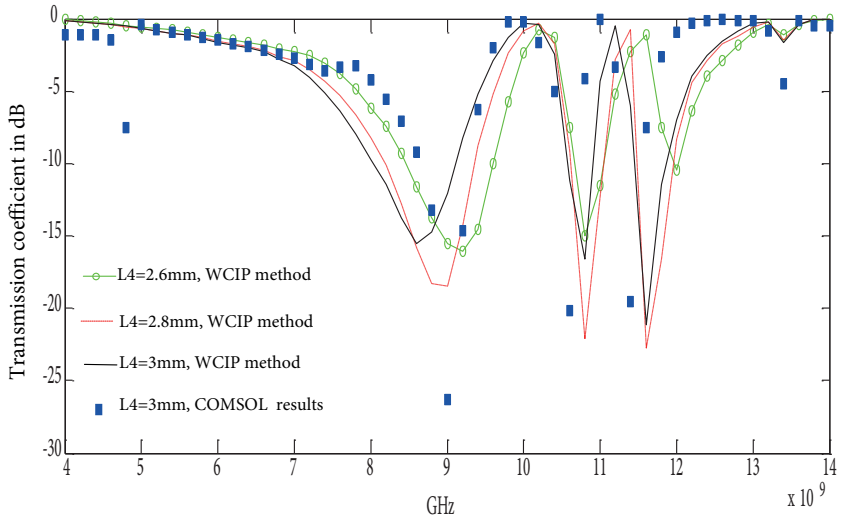

Figure 4. Variation of the transmission power versus frequency.

tuned, whereas at the same time L_4 can be considered as a way for fine-tuning of the FSS central and highest resonant frequencies.

Figure 5 shows the transmission coefficient of the joined split-ring FSS using the WCIP method when the FSS is fed with an x polarized normal plane wave. Increasing L_8 from 7.5 mm to 10.5 mm leads to the shifting down of the highest resonant frequency from 11.6 GHz to 11.2 GHz. Moreover, an enhanced rejecting band of 0.65 GHz at –10 dB is observed when L_8 equals 10.5 mm. The differences between the WCIP results and the COMSOL Multiphysics simulation results are due to the limited number of points used to define the FSS interface in conjunction with the number of iterations used to stop the procedure. For $L_8 = 10.5$ mm, a single resonance exist. The upper two resonant frequencies observed for $L_8 = 6$ mm, $L_8 = 7$ mm, and $L_8 = 9.5$ mm are brought nearer to each other by increasing L_8 to 10.5 mm. As a result, the observed two upper resonances overlap to create a single resonant region with an enhanced rejecting band.

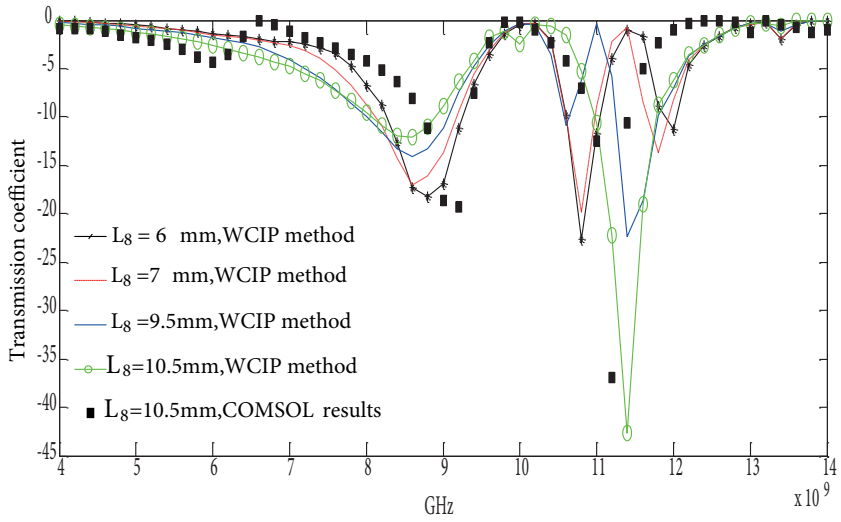

Figure 5. Variation of the transmission power versus frequency.

Figure 6 represents the transmitted power versus the operating frequency of the joined split-ring FSS for

different values of L_1 as the FSS is fed with an x polarized normally incident plane wave. An increase in the upper coupling strip of length L_1 from 8.5 mm to 11.5 mm results in decreasing the central resonant frequency. When the upper coupling strip length is 11.5 mm, an enhanced band of 2.1 GHz centered at about 8.8 GHz is observed.

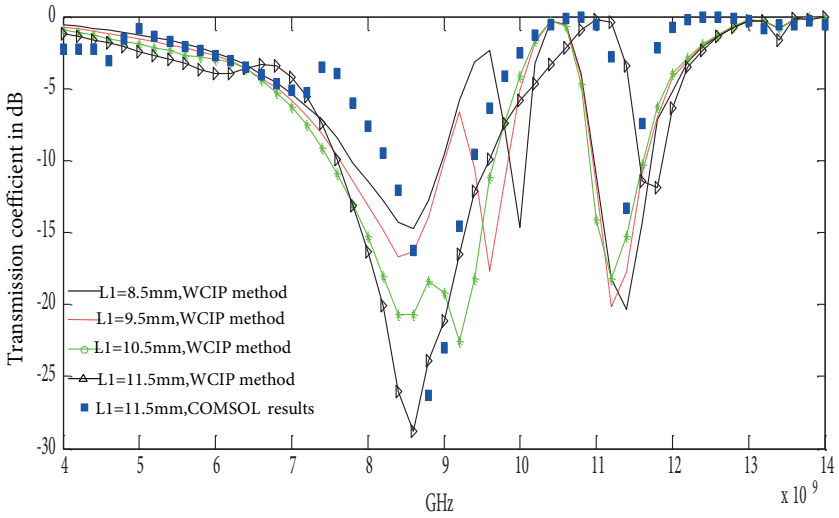

Figure 6. Variation of the transmission power versus frequency.

The choice of the (L_1, L_4) pair is done in such a way to obtain an enhanced band resulting from bringing the FSS lowest frequency and the central resonant frequency close to each other to overlap. In Figure 7 the transmitted power of the joined split-ring FSS structure is plotted for different pair values (L_1, L_4) varying from (10.5 mm, 0.6 mm) to (11.5 mm, 1 mm) and then varying to (12.5 mm, 1.2 mm), fed with an x polarized normally incident plane wave. An enhanced band of about 2.2 GHz at –10 dB and centered at about 8.5 GHz is observed when the (L_1, L_4) pair is taken equal to (12.5 mm, 1.2 mm). When the (L_1, L_4) pair is taken equal to (10.5 mm, 0.6 mm), the enhanced band center frequency is moved up until about 9.5 GHz with the bandwidth remaining approximately unchanged.

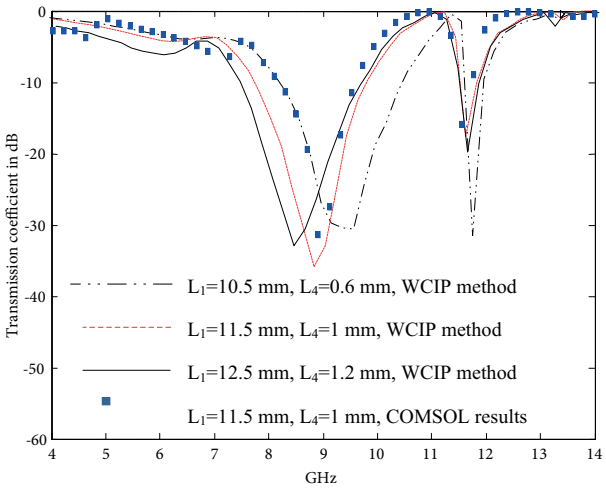

Figure 7. Variation of the transmission power versus frequency.

The current density is represented for the three resonant frequencies in Figures 8, 9, and 10 versus the interface plane (Ω) for the joined split-ring FSS structure of Figure 2. The figures show that the boundary conditions are satisfied for all the metallic and dielectric domains being zero on the dielectric domain and concentrated on the metallic strip edges.

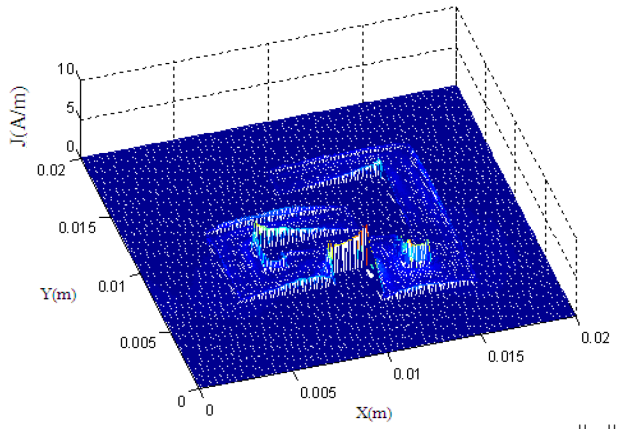

Figure 8. Distribution of the electric current density $\left\|\vec{J}\right\|$ in $\mathrm{A/m^2}$ in terms of interface Ω at 9 GHz.

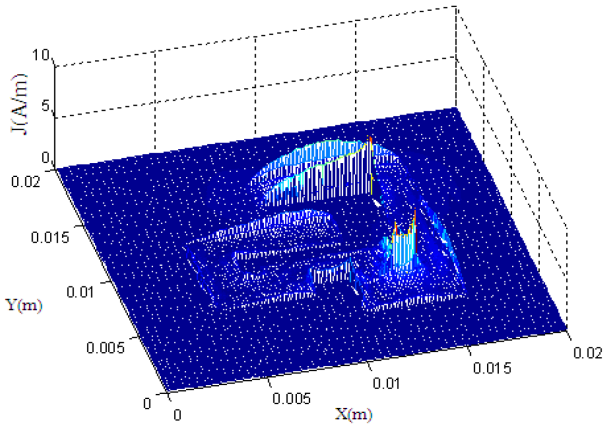

Figure 9. Distribution of the electric current density $\left\|\vec{J}\right\|$ in $\mathrm{A/m^2}$ in terms of interface Ω at 10.5 GHz.

Bringing the notch to the center of the lower coupling strip, as shown in Figure 11, leads to a modified quasi-square joined split-ring characterized by four rejecting bands when the structure is excited with an x polarized normal incident plane wave as shown in Figure 12.

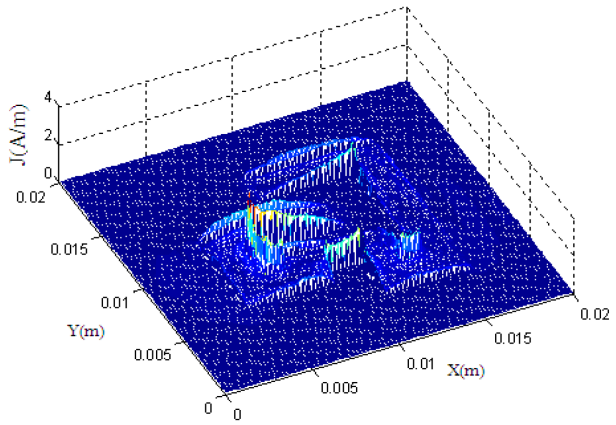

Figure 10. Distribution of the electric current density $\left\|\vec{J}\right\|$ in $\mathrm{A/m^2}$ in terms of interface Ω at 11.5 GHz.

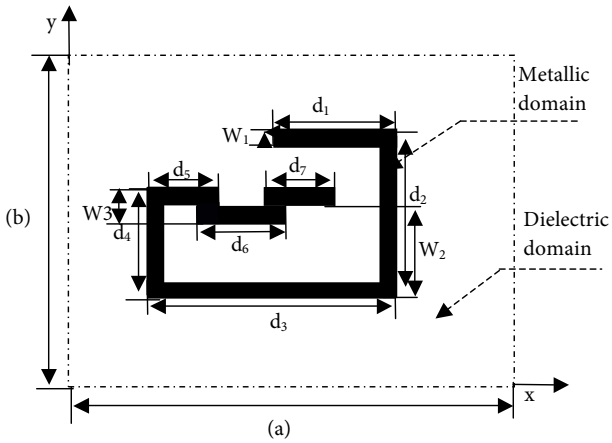

Figure 11. Geometry of the modified unit cell.

Depicted in Figure 12 is the transmitted power versus the operating frequency for the modified quasi-square joined split-ring FSS of Figure 11 obtained by the WCIP method and COMSOL Multiphysics 4.3.b. The dimensions of the unit cell modified FSS are given in Table 2. Four resonances occur at about 6.7 GHz, 8.5 GHz, 10.6 GHz, and 13 GHz.

Figure 13 represents the transmitted power versus the operating frequency of the modified quasi-square joined split-ring FSS for different values of d_1 as the FSS is fed with an x polarized normally incident plane

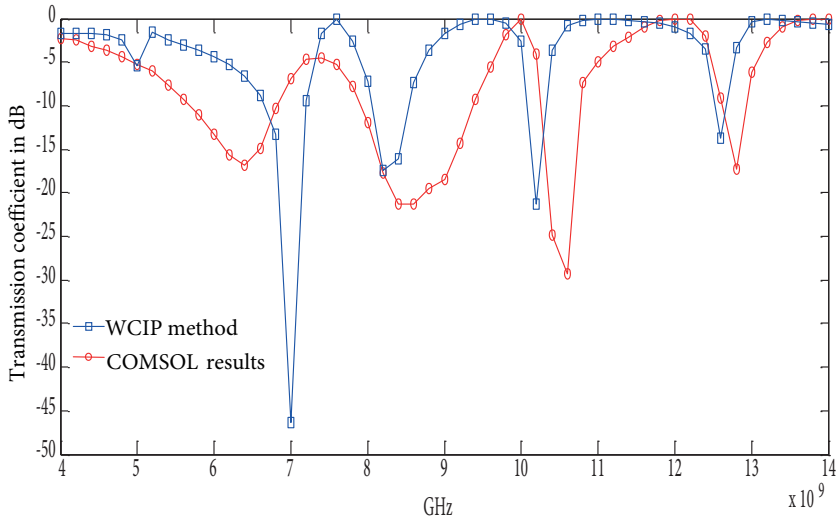

Figure 12. Variation of the transmission power versus frequency.

Table 2. Parameters of the modified FSS unit cell.

W_1 $[mm]$	W_2 $[mm]$	W_3 $[mm]$	d_1 $[mm]$	d_2 $[mm]$	d_3 $[mm]$	d_4 $[mm]$	d_5 $[mm]$	d_6 $[mm]$	d_7 $[mm]$	h $[mm]$	ε_r
2	2.5	4	5.5	8.7	13	6.5	4.2	3.8	2.8	1	4.4

wave. Only the highest resonant frequency is considerably changed where it is shifted down from 13.3 GHz to 12.2 GHz when d_1 is varied from 5 mm to 6.5 mm. When the length d_1 is varied to 6.5 mm, an enhanced band equal to about 0.8 GHz at –10 dB and centered at about 12.2 GHz is observed.

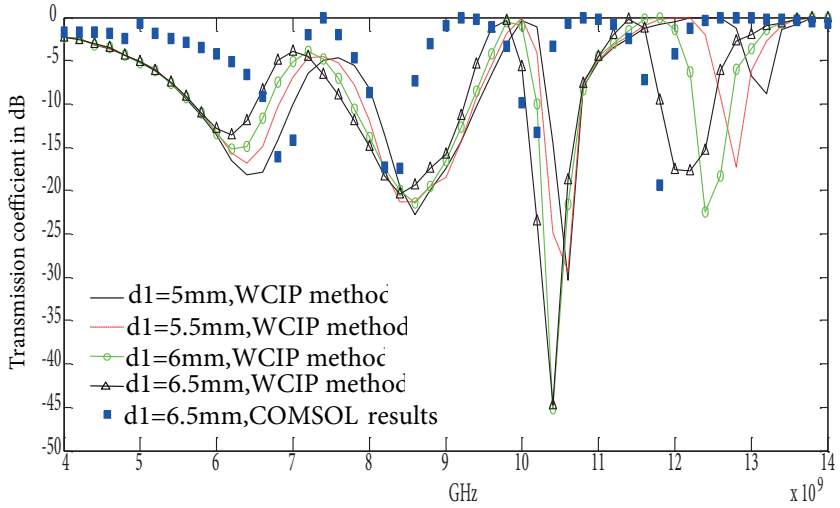

Figure 13. Variation of the transmission power versus frequency.

Figure 14 shows the obtained transmission coefficient of the same FSS versus the operating frequency for different values of the upper strip width W_1 as the FSS is excited with a source plane wave polarized in the x direction. The resonant frequency centered at 10.1 GHz obtained for $W_1 = 4$ mm is inversely proportional to W_1.

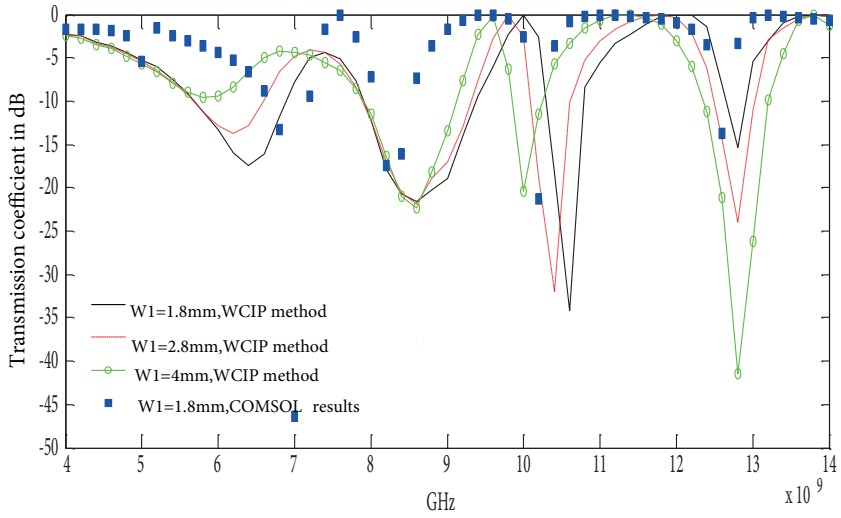

Figure 14. Variation of the transmission power versus frequency.

In Figure 15 the transmission coefficient of the modified FSS excited with an x polarized normal plane wave is presented. Only the rejecting band centered at about 8.5 GHz is moved up to 9.5 GHz by varying simultaneously strip width W_1 from 3.5 mm to 2 mm and length W_2 from 1 mm to 2.5 mm.

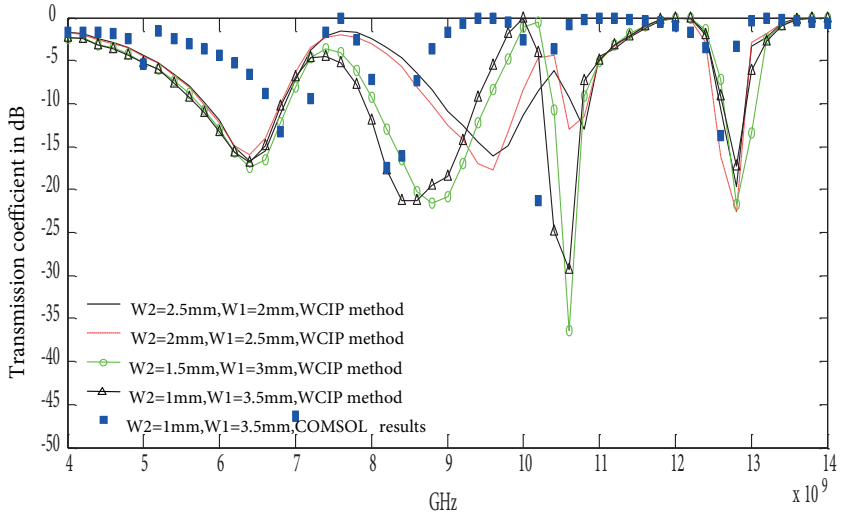

Figure 15. Variation of the transmission power versus frequency.

5. Conclusion

In this paper a joined split-ring FSS is proposed and experimentally verified. This structure provides three rejecting bands when the incident plane wave is polarized in the x direction. The dimensions responsible for independently varying the resonant frequencies of the FSS are determined to give rise to two possible nonsimultaneous enhanced bands centered at two different adjustable resonant frequencies. The proposed structure also shows one rejecting band when the FSS is excited in the $y$direction. To end with an FSS with four rejecting bands, the notch is moved at the center of the lower metallic parallel strip. The parametric study of the novel FSS allows the determination of the dimensions affecting three resonant frequencies among four

existing resonant frequencies and one adjustable enhanced band can be obtained when two adjacent rejecting bands are sufficiently moved towards each other. The results show good agreement between WCIP results, simulations results obtained by COMSOL, and measurements.

References

[1] Kim DH, Choi JI. Design of a multiband frequency selective surface. ETRI J 2006; 28: 506-508.

[2] Pasian M, Ettorre M, Neto A, Monni S, Gerini G. Frequency selective surface for extended bandwidth backing reflector functions. IEEE T Antenn Propag 2010; 58: 43-50.

[3] Bera S. Design of novel shaped compact frequency selective surface with dual band applications. International Journal of Electronics & Communication Technology 2013; 4: 29-32.

[4] Cuthbert AM, Elesherbeni AZ, Smith CE, Huang CP, Lee K. Tapered meander slot antenna for dual band personal wireless communication systems. Microw Opt Techn Let 2003; 36: 381-385.

[5] Titaouine M, Raveu N, Gomes Neto A, Baudrand H. Electromagnetic modeling of quasi-square open metallic ring frequency selective surface using the wave concept iterative procedure. ETRI J 2009; 31: 77-79.

[6] Titaouine M, Gomes Neto A, Baudrand H, Djahli F. WCIP method applied to active frequency selective surfaces. Journal of Microwaves, Optoelectronics and Electromagnetic Applications 2007; 6: 1-16.

[7] Tellache M, Lamhene Y, Haraouiba B, Baudrand H. An numerical based iterative process to characterize microwave planar circuits. International Journal of Computing 2008; 7: 86-94.

[8] Basaran SC, Sertel K. Dual wideband CPW- fed split-ring monopole antenna with split-ring resonators. Microw Opt Techn Let 2013; 55: 2088-2092.

[9] Sahay J, Goutham D, Tanweer, Kumar S. A novel compact ultra wide band filter for reconfigurable notches. Microw Opt Techn Let 2015; 57: 88-91.

[10] Alhzzoury IA. Contribution à la modélisation des structures SIW et SINRD pour application micro-ondes et télécommunication. Toulouse, France: Institut National Polytechnique de Toulouse, 2013 (in French).

[11] Adoui I, Titaouine M, Choutri H, Boudrand H. WCIP method as applied to rectangular patch multilayer periodic structure iteration. International Journal of Computer Science and Electronics Engineering 2014; 2: 185-188.

[12] Aroussi S, Latrach L, Sboui N, Gharsallah A, Gharbi A, Baudrand H. Efficient analysis of complex FSS structure using the WCIP method. Journal of Electromagnetic Analysis and Applications 2012; 3: 447-451.